DOI: 10.13009/EUCASS2019-1020

DOI: ADD DOINUMBER HERE

Numerical Simulation of the Subsonic Jet Noise with Installation Effect

Junhui Gao⋆† *and Xiaodong Li*⋆
⋆*School of Energy and Power Engineering, BeiHang University*
Xueyuan Road 37, Haidian District, Beijing, 100191, P. R. China
gaojhui@buaa.edu.cn · lixd@buaa.edu.cn
†Corresponding author

Abstract

In this study, the jet noise with installation effect is simulated with a high order computational aeroacoustics solver. A convergent nozzle with exit diameter (D) equal to 2.54cm is placed under a NACA0012 airfoil. The fully expanded Mach number of the jet is 0.9, and the reservoir temperature ratio is 1. In order to study the influence of their relative positions on jet noise, the location of the airfoil is changed both in the x and radial directions. In the simulation, the spectral difference (SD) method on hexahedral element is utilized for spatial descritization. The multi-time step method based on the the optimized Adams-Bashforth scheme is implemented in the SD code for time integration to speed up the simulation. The Large-Eddy-Simulation (LES) method based on the Wall-adapting local eddy-viscosity (WALE) turbulence model is applied in the simulation. The flow fields, including the mean axial velocity, turbulent kinetic energy, RMS of the velocity perturbations are analyzed to show the installation effect. To obtain the far field noise, the permeable Ffowcs Williams-Hawkings (FW-H) integration formula including only the monopole and dipole sources for a moving surface is utilized. The far field noise spectra at different observer angles are compared with the experimental data. The effect of the axial and radial positions of the airfoil on the far field noise are presented and analyzed.

1. Introduction

Jet noise has long been a fascinating subject of aeroacoustics research. A large number of investigations on jet noise have been conducted for various aspects during the past six decades, and great advances have been achieved for the understanding of jet noise generation mechanism. For the traditional under the wing mounted engine, jet noise suffers an installation effect, which makes the jet noise bigger than isolated jet. The installation effect on jet noise had been noticed since 1970s. A considerable amount of researches[23,28–30] was conducted in NASA's Lewis Research Center on jet noise shielding by airframe surface. Their work focused on understanding the effects of nozzle size and location relative to the wing using engine-over-the-wing (OTW) configurations with convergent circular nozzles that operated at different velocities. Wang[31] studied systematically the jet noise with installation effect with experiments. Other researchers, such as [4,5,11,18,20] also carried out lots of experiments for this problem. According to Von Glahn et al.,[29] the jet noise shielding by airframe surface reduced the sound pressure level for middle and high frequencies, but amplified noise at low frequencies. With the help of advanced testing techniques and algorithm such as beamforming, researchers now can identify two sources caused by installation effect. One was believed to be generated by the interaction between the jet flow and the trailing edge. The second was attributed to scrubbing noise that results from the jet flow contacting the shielding surface. And with the help of flow visualization, a connection of flow and sounding mechanism can be made. Even though lots of experiments have been performed about jet noise with installation effect, researchers still don't have a clear understanding of its mechanism, because the physical phenomenon of turbulence is still unclear.

Computational aeroacoustics (CAA) have advanced significantly in recent years, and different levels of numerical approaches have been developed. Many researchers have studied jet noise with various numerical methods, and great advances have been made in prediction and understanding of jet noise. But few works[21,22] are conducted on jet with installation effect. The complex geometry of the jet-under-wing configuration makes its difficult for accurate prediction, and the huge computation resource requirement is also another obstacle. The main objective of this study is aimed at predicting accurately the noise from a subsonic jet with installation effect using the high order spectral difference method, and analyzing the installation effect on the flow field and the far field noise.

DOI: 10.13009/EUCASS2019-1020

In the next section, the numerical methods, including the SD method, time marching scheme, boundary conditions, and the far field noise integration method, are introduced briefly. The numerical results are presented in section 3. Section 4 gives the conclusion of this work.

2. Numerical Methods

2.1 Spectral difference method

In this study, the spectral difference method[16,25] on hexahedral grids is used for spatial discretization. This method has been used by the present authors for simulating of tandem cylinder flow, and the noise from high-lift configuration.[8,10] Consider the three dimensional compressible Favre filtered Navier-Stokes equations in conservative form

$$\frac{\partial Q}{\partial t}+\frac{\partial F}{\partial x}+\frac{\partial G}{\partial y}+\frac{\partial H}{\partial z}=0 \tag{1}$$

where Q is the vector of conserved variables; F, G and H are the total fluxes including both inviscid and viscous flux vectors. The details of the governing equations are not included here for brevity.

In the numerical simulation with SD method, the physical domain is divided into Ne non-overlapping elements. To achieve an efficient implementation, all elements in the physical domain (x,y,z) are transformed into a standard cubic element $(0\leqslant\xi\leqslant 1, 0\leqslant\eta\leqslant 1, 0\leqslant\zeta\leqslant 1)$ with the following formula,

$$\begin{pmatrix} x \\ y \\ z \end{pmatrix}=\sum_{i=1}^{k} M_i(\xi,\eta,\zeta)\begin{pmatrix} x_i \\ y_i \\ z_i \end{pmatrix} \tag{2}$$

where k is the total number of points used to define the physical element, (x_i,y_i,z_i) are the Cartesian coordinates of those points, and $M_i(\xi,\eta,\zeta)$ are the shape functions. For the quadrilateral element with straight edges, k is equal to 4, and for the hexahedral element, k is equal to 8. The metrics and the Jacobian of the transformation can be computed for each element. The Jacobian can be expressed as

$$J=\begin{pmatrix} x_\xi & x_\eta & x_\zeta \\ y_\xi & y_\eta & y_\zeta \\ z_\xi & z_\eta & z_\zeta \end{pmatrix} \tag{3}$$

The governing equations in the physical domain are transferred into the computational domain. The tranformed equations are

$$\frac{\partial \tilde{Q}}{\partial t}+\frac{\partial \tilde{F}}{\partial \xi}+\frac{\partial \tilde{G}}{\partial \eta}+\frac{\partial \tilde{H}}{\partial \zeta}=0 \tag{4}$$

where $\tilde{Q}=|J|\,Q$ and

$$\begin{aligned} \tilde{F}&=(F\xi_x+G\xi_y+H\xi_z)\,|J| \\ \tilde{G}&=(F\eta_x+G\eta_y+H\eta_z)\,|J| \\ \tilde{H}&=(F\zeta_x+G\zeta_y+H\zeta_z)\,|J| \end{aligned} \tag{5}$$

For the quadrilateral cell in 2D or hexahedral element in 3D, the solution points in one dimensional are selected to be the Chebyshev-Gauss points,

$$x_s(i)=0.5(1-\cos(\frac{2i-1}{2N}\pi)),\qquad i=1,\cdots,N \tag{6}$$

where N is the order of the SD method. The Legendre-Gauss-quadrature (L-G-Q) points plus two end points as suggested by Huynh[14] and Van den Abeele et al.[1] are used for flux points,

$$P_n(\xi)=\frac{2n-1}{n}(2\xi-1)P_{n-1}(\xi)-\frac{n-1}{n}P_{n-2}(\xi) \tag{7}$$

The locations of these L-G-Q flux points are the roots of equation $P_n(\xi)=0$. The distribution of the two dimensional solution and flux points for the 4th order SD method is shown in Fig. 1. Using the solutions at N solution points, a

DOI: 10.13009/EUCASS2019-1020

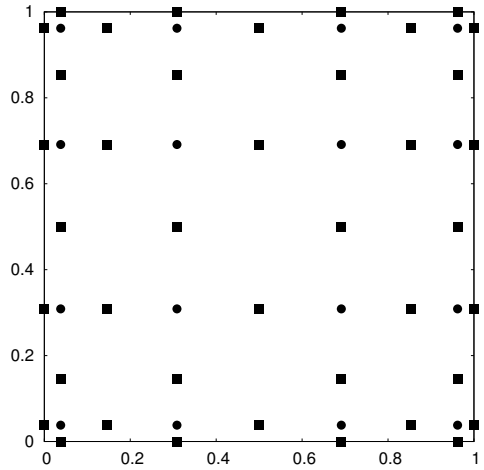

Figure 1: Distribution of the two dimensional solution and flux points for the 4th order SD method (• Solution Points; ■ Flux Points).

degree $N-1$ polynomial in each coordinate direction can be built with the Lagrange formula,

$$h_i(x) = \prod_{\substack{r=1 \\ r\neq i}}^{N} \frac{x - x_s(r)}{x_s(i) - x_s(r)}, \qquad i = 1, \cdots, N \tag{8}$$

Using the fluxes at $N+1$ flux points, a degree N polynomial in each coordinate direction can be built with the Lagrange formula,

$$l_{i+1/2}(x) = \prod_{\substack{r=0 \\ r\neq i}}^{N} \frac{x - x_f(r)}{x_f(i) - x_f(r)} \tag{9}$$

The conservative variables in the standard element can be constructed with

$$\tilde{Q}(\xi,\eta,\zeta) = \sum_{k=1}^{N}\sum_{j=1}^{N}\sum_{i=1}^{N} \tilde{Q}_{i,j} h_i(\xi)\, h_j(\eta)\, h_k(\zeta) \tag{10}$$

The flux can also be computed similarly

$$\begin{aligned}
\tilde{F}(\xi,\eta,\zeta) &= \sum_{k=1}^{N}\sum_{j=1}^{N}\sum_{i=0}^{N} \tilde{F}_{i+1/2,j,k} l_{i+1/2}(\xi)\, h_j(\eta)\, h_k(\zeta) \\
\tilde{G}(\xi,\eta,\zeta) &= \sum_{k=1}^{N}\sum_{j=0}^{N}\sum_{i=1}^{N} \tilde{G}_{i,j+1/2,k} h_i(\xi)\, l_{j+1/2}(\eta)\, h_k(\zeta) \\
\tilde{H}(\xi,\eta,\zeta) &= \sum_{k=0}^{N}\sum_{j=1}^{N}\sum_{i=1}^{N} \tilde{G}_{i,j,k+1/2} h_i(\xi)\, h_j(\eta)\, l_{k+1/2}(\zeta)
\end{aligned} \tag{11}$$

The reconstructed fluxes are only element-wise continuous, and discontinuous across element interfaces. For the inviscid flux, a Riemann flux solver is used to compute the common flux at interfaces to ensure conservation and stability. Usually the Rusanov solver[24] is utilized to compute the interface fluxes:

$$\hat{\mathbf{F}^{\mathbf{inv}}} = \frac{1}{2}[(\mathbf{F^{inv}}_L + \mathbf{F^{inv}}_R)\cdot \mathbf{n} - \lambda(Q_R - Q_L)] \tag{12}$$

where Q and $\mathbf{F^{inv}}$ are the conserved variables and inviscid fluxes, the subscript R and L represent the right and left sides of the edge interfaces respectively, $\mathbf{n}$ is the normal vector of the cell interface, $\lambda = |V_n| + c$ is an upper bound of the absolute values of the characteristic speed. V_n is the fluid velocity normal to the edge interface and c is the sound speed.

The steps to compute the inviscid flux can be summarized as follows,

DOI: 10.13009/EUCASS2019-1020

1. Given the conservative variables on the solution points, compute the conservatives on the flux points with Eq. (10);
2. Compute the inviscid fluxes on flux points with the conservative variables calculated in step 1;
3. Compute the common fluxes with Rusanov/Roe flux solver;
4. The derivatives of the fluxes on solution points can be computed with the following equations, using the derivatives of Lagrange interpolation formula;

$$
\begin{aligned}
(\frac{\partial \tilde{F}}{\partial \xi})_{i,j,k} &= \sum_{r=0}^{N} \tilde{F}_{r+1/2,j,k} l'_{r+1/2}(\xi_i) \\
(\frac{\partial \tilde{G}}{\partial \eta})_{i,j,k} &= \sum_{r=0}^{N} \tilde{G}_{i,r+1/2,k} l'_{r+1/2}(\eta_j) \\
(\frac{\partial \tilde{H}}{\partial \zeta})_{i,j,k} &= \sum_{r=0}^{N} \tilde{H}_{i,j,r+1/2} l'_{r+1/2}(\zeta_k)
\end{aligned}
\tag{13}
$$

Since the viscous fluxes are the function of conservative variables and their gradients, the following steps are used to compute their derivatives,

1. Compute the conservative variables Q_f on flux points from solution points based on Eq. (10);
2. Compute the common conservative variables on element interfaces with a simple algebraic average $\bar{Q}_f = \frac{1}{2}(Q_f^L + Q_f^R)$, and apply the boundary conditions to the conservative variables on flux points at boundary elements;
3. Based on Eq. (13), calculate the gradients ∇Q with $\bar{Q}_f$ obtained in the previous step; where $\nabla = \left\{ \begin{array}{c} Q_x \\ Q_y \\ Q_z \end{array} \right\}$, $Q_x = \frac{\partial Q}{\partial \xi}\xi_x + \frac{\partial Q}{\partial \eta}\eta_x + \frac{\partial Q}{\partial \zeta}\zeta_x$. Similar with Q_y and Q_z;
4. Reconstruct the ∇Q on flux points with Eq. (10), and calculate the average value on element interfaces, $\overline{\nabla Q}_f = \frac{1}{2}(\nabla Q_f^L + \nabla Q_f^R)$;
5. Compute the viscous fluxes on flux points with $\bar{Q}_f$ and $\overline{\nabla Q}_f$;
6. Compute the derivatives of the viscous fluxes with Eq. (13);

2.2 WALE turbulence model

In this study, the Large Eddy Simulation (LES) method is used to simulate the turbulence, which only resolves the larger scales of motion and thus allows for the use of coarser meshes. The effect of the unresolved or sub-grid-scale (SGS) dynamics on the solution is accounted for by a SGS model for the subgrid-scale stress τ_{ij}, which is added to the viscous stress tensor σ_{ij},

$$
\sigma_{ij} = 2\mu S_{ij}^d + \tau_{ij} \tag{14}
$$

$$
S_{ij}^d = \frac{1}{2}(\frac{\partial \tilde{u}_i}{\partial x_j} + \frac{\partial \tilde{u}_j}{\partial x_i} - \frac{2}{3}\delta_{ij}\frac{\partial \tilde{u}_k}{\partial x_k}) \tag{15}
$$

where $\tilde{u}_i (i = 1, 2, 3)$ is the resolved velocities in each coordinate direction. The Wall-Adapting Local Eddy-Viscosity (WALE) model by Nicoud & Ducros[19] is utilized in the simulation. In the model, the sub-grid-scale stress τ_{ij} is computed with the following formula,

$$
\tau_{ij} = 2\mu_t S_{ij}^d \tag{16}
$$

$$
\mu_t = \bar{\rho} C_w^2 \Delta^2 \frac{(s_{ij}^d s_{ij}^d)^{\frac{3}{2}}}{(S_{ij}^d S_{ij}^d)^{\frac{5}{2}} + (s_{ij}^d s_{ij}^d)^{\frac{5}{4}}} \tag{17}
$$

DOI: 10.13009/EUCASS2019-1020

where μ_t is the modeled turbulence eddy viscosity, and s_{ij}^d is the traceless symmetric part of the square of the resolved velocity gradient tensor $g_{ij} = \frac{\partial \tilde{u}_i}{\partial x_j}$, namely $s_{ij}^d = \frac{1}{2}\left(g_{ij}^2 + g_{ji}^2 - \frac{2}{3}\delta_{ij}g_{kk}^2\right)$ with $g_{ij}^2 = g_{ik}g_{kj}$. $C_w = 0.5$ is the model coefficient, and Δ is a measure of the grid cutoff length-scale, which is computed with

$$\Delta = \left[\frac{|det(J(\xi))|}{N^3}\right]^{\frac{1}{3}} \tag{18}$$

where N is the order of the SD scheme, and $det(J(\xi))$ is the determinant of the Jacobian matrix in Eq. (3).

2.3 Multi-time-step integration method

In this study, the multi-time step method[17] based on the the optimized Adams-Bashforth scheme[27] is implemented in our SD code for time integration to speed up the simulation. The commonly used high order explicit time marching method (such as Low-Dissipation & Low-Dispersion Runge-Kutta scheme[13]) is not used because of the limitation of small time step which is determined by the smallest cell size in the turbulence boundary layer. The advantage of multi-time step method is it allows different time steps for cells with different sizes. This would speed up the computation greatly. The spectral difference solver with multi-time-step method has been validated by the present authors and applied to simulate the aeroacoustic problems with multiple scales,[6,7,9] and the results demonstrated that it is accurate and efficient for unsteady simulation with multiple flow scales.

2.4 Boundary conditions

Boundary condition is an key element of a CAA approach. As sketched in Fig. 2, the Perfectly matched layer boundary condition[12] of nonlinear Euler equations is implemented at the left boundary outside the nozzle. The radiation boundary conditions in the 3D form by Bogey & Bailly[2] suitable for weakly non-uniform mean flows are applied at the far field boundary regions. At the downstream boundary region where $Ma \geqslant 0.001$, the modified outflow boundary condition of Tam & Dong[15,26] in 3D form is used. The no-slip wall boundary condition is used on the nozzle and the airfoil wall surfaces. At the inlet of the nozzle, the inflow boundary condition based on the Riemann invariant characteristic method is applied.

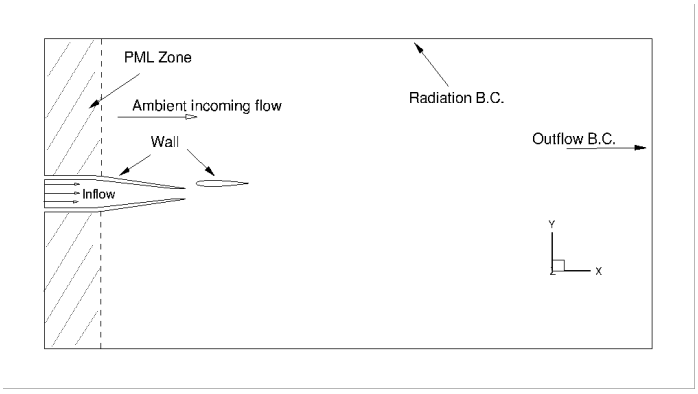

Figure 2: The boundary conditions implemented in the simulation.

2.5 FW-H Integration Method

The far field jet noise is the focus for industry. It is time exhausted and un-economical to compute the far field sound with the LES solver by extending the near field fine grid to the far field. A feasible way to calculate far field sound is the Ffowcs Williams-Hawkings integration method.[3] Since the integration surface in this study is sufficiently large to include all the non-linear flow field, the quadrupole term can be neglected. The permeable FW-H formula including

DOI: 10.13009/EUCASS2019-1020

only the monopole and dipole sources for a moving surface can be written as,

$$p'(x,t) = p'_T(x,t) + p'_L(x,t) \tag{19}$$

$$\begin{aligned} 4\pi p'_T(x,t) &= \int_{f=0}\left[\frac{\rho_0(\dot{U}_n + U_{\dot{n}})}{r(1-M_r)^2}\right]_{ret} \mathrm{d}S \\ &+ \int_{f=0}\left[\frac{\rho_0 U_n(r\dot{M}_r + c(M_r - M^2))}{r^2(1-M_r)^3}\right]_{ret} \mathrm{d}S \end{aligned} \tag{20}$$

$$\begin{aligned} 4\pi p'_L(x,t) &= \frac{1}{c}\int_{f=0}\left[\frac{\dot{L}_r}{r(1-M_r)^2}\right]_{ret} \mathrm{d}S \\ &+ \int_{f=0}\left[\frac{L_r - L_M}{r^2(1-M_r)^2}\right]_{ret} \mathrm{d}S \\ &+ \frac{1}{c}\int_{f=0}\left[\frac{L_r(r\dot{M}_r + c(M_r - M^2))}{r^2(1-M_r)^3}\right]_{ret} \mathrm{d}S \end{aligned} \tag{21}$$

where $f = 0$ and $[...]_{ret}$ means integration at the retarded time, p'_T and p'_L are the thickness and loading noise term respectively.

3. Numerical Results and Discussions

3.1 Configurations

A convergent nozzle with exit diameter (D) equal to 2.54cm is placed under a NACA0012 airfoil. The nozzle exit lip thickness is about 0.008D. The chord length of the airfoil is 5D, and the thickness is 0.6D. At baseline position the nozzle exit centre is 1.25D under the airfoil leading edge, as shown in Fig. 3. In order to study the influence of their relative positions on jet noise, the airfoil has 3 positions in x direction and 3 positions in y direction. They are $0, 0.5D$ and $1.0D$ in the x direction and $-0.25D, 0$ and $0.25D$ in the y direction relative to the baseline position. In all the following contents, the relative coordinates of the airfoil leading edge are used to represent the position of the airfoil. To simplify the simulation, the airfoil is extended to the full span of the whole computational domain.

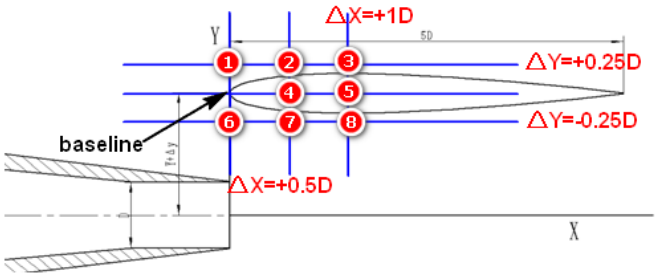

Figure 3: Illustration of the position of the airfoil.

The fully expanded Mach number (M_j) of the jet is 0.9, and the reservoir temperature ratio is 1. The ambient air Mach number (Ma_∞) is 0 to simulate the jet in static condition. The Reynolds number ($Re_D = \frac{\rho_j U_j D}{\mu}$) based on the jet velocity (U_j) and the nozzle diameter (D) is about 6.5×10^5.

The computational domain is extended from -13D to 45D in the x direction, and -15D to 15D in both the y and z directions. Fine mesh is distributed in the wall region and shear layer of the jet. Totally there are about 576,000 hexahedral elements used in the simulation. There are about 15.5 million degree-of-freedom (DOFs) for the simulation with the third order SD scheme. A slice of mesh in $x-y$ plane is shown in Fig. 4(a), and its enlarged view in the region around the airfoil is plotted in Fig. 4(b). It can be found that the mesh points are concentrated in the core area of the jet plume and around the airfoil.

3.2 Flow Fields

The instantaneous pressure fields at x-y plane of the jet are shown in Fig. 5. The effect of the airfoil positions on the instantaneous pressure fields can be observed in Fig. 5. The radiated sound waves in the upstream and downstream

DOI: 10.13009/EUCASS2019-1020

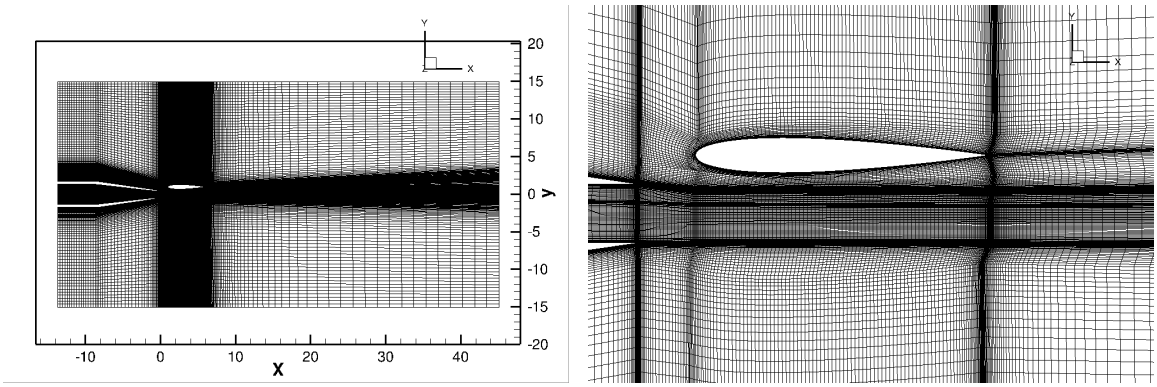

(a) (b)

Figure 4: Mesh used in the simulation.

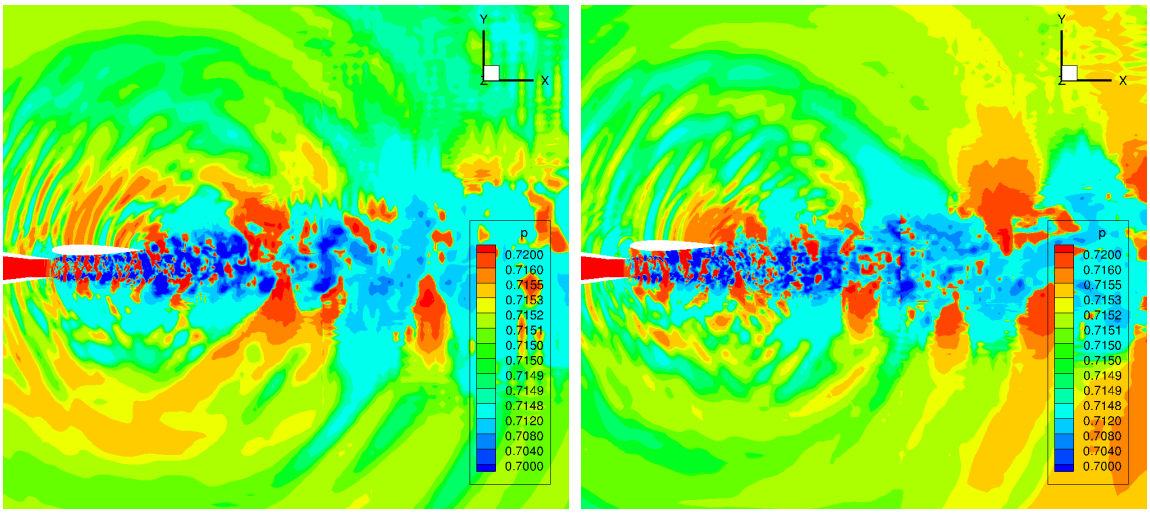

(a) $(0, 1.0D)$ (b) $(0, 1.25D)$

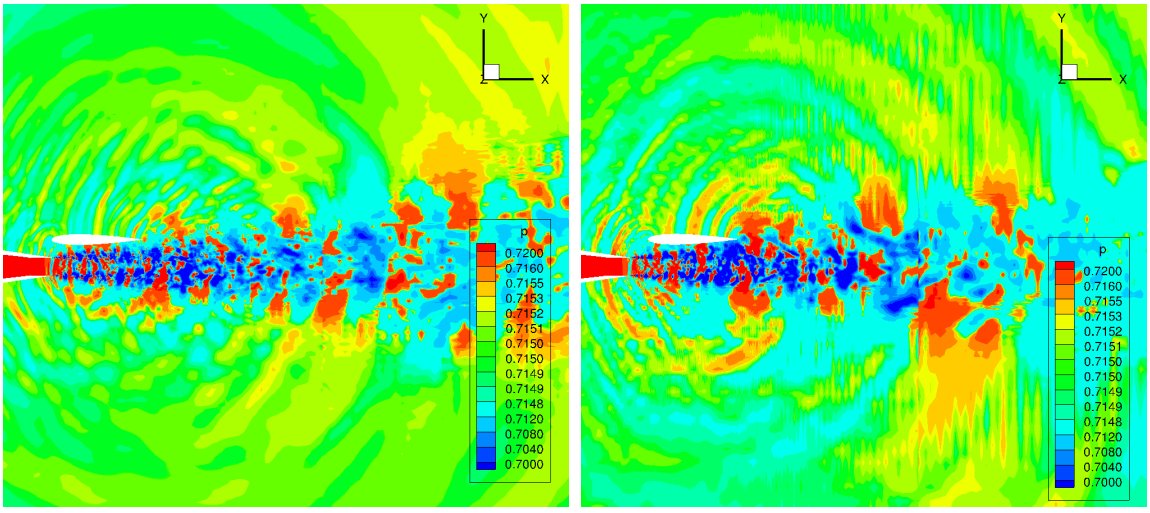

(c) $(0, 1.5D)$ (d) $(1, 1.5D)$

Figure 5: Instantaneous pressure contours in the $x - y$ plane, the airfoil with different positions.

DOI: 10.13009/EUCASS2019-1020

directions can be observed clearly. It can also be found that stronger noise is radiated in the un-shielded side of the jet, especially in the downstream direction. Strong noise generated from the trailing edge of the airfoil can be observed in Fig. 5(a), in which the gap between jet and the airfoil is the smallest. Therefore the jet has a strong interaction with the airfoil trailing edge and generates strong noise. For the results of the airfoil with radial positions equal to 1.25D and 1.5D, as shown in Fig. 5(b) and 5(c), the radiated noise is weaker clearly because of larger gap. Comparing the results of the airfoil with different axial positions, it is found that stronger noise is generated in Fig. 5(d) because the trailing edge of the airfoil has stronger interaction with the shear layer.

The contours of z vorticity in the $x-y$ plane of the jet are plotted in Fig. 6. For the three figures in the left column, the axial position of the airfoil is fixed to be 0, and the y position of the airfoil is changed from 1.0D to 1.5D. It is clearly shown that the vorticities of the jet have a strong interaction with the airfoil in Fig. 6(a), but the interaction is becoming weaker with increasing of the gap between the airfoil and the jet. For the three figures in the right column of Fig. 6, the axial position of the airfoil is fixed to $1.0D$. Similar with the results shown in the left column, the interaction between the jet and the airfoil becomes weaker by increasing the gap. Comparing the figures in the left and right column with the same radial position, for example, Fig. 6(e) and 6(f), stronger interaction can be observed for the case with the airfoil located further downstream.

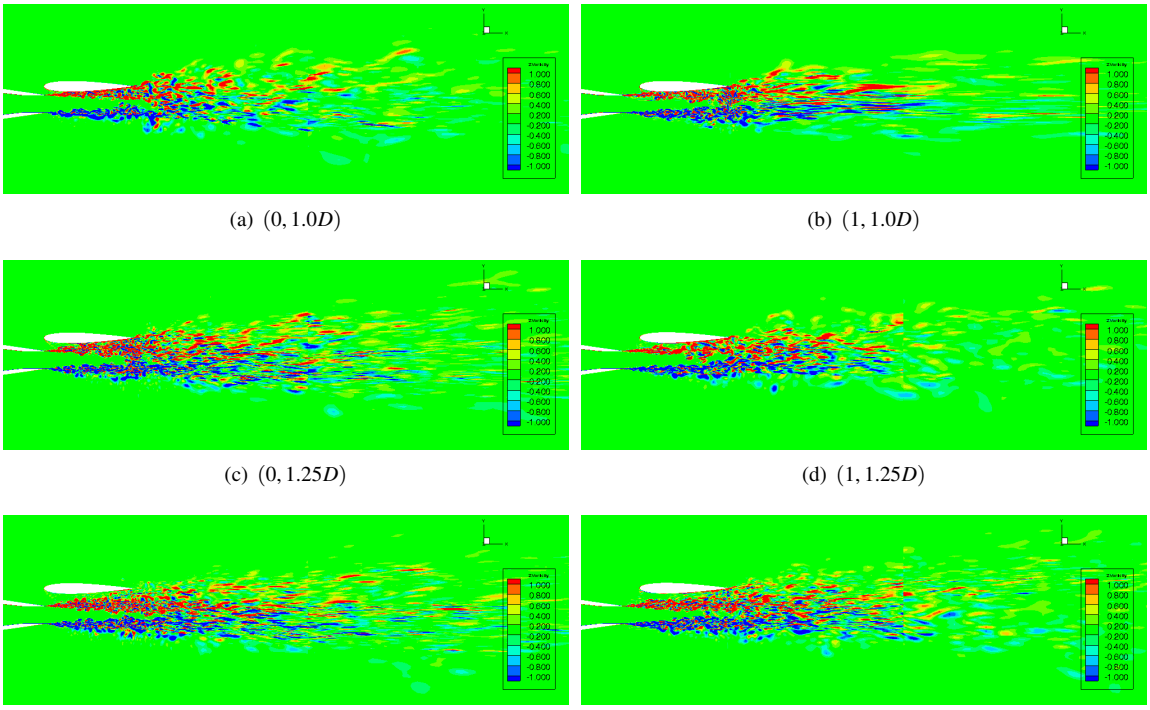

(a) $(0, 1.0D)$ (b) $(1, 1.0D)$

(c) $(0, 1.25D)$ (d) $(1, 1.25D)$

(e) $(0, 1.5D)$ (f) $(1, 1.5D)$

Figure 6: Contours of z vorticity in the x-y plane, the airfoil with different positions.

The mean flow field is obtained with a long time average. Fig. 7 shows the mean axial velocity fields of the jet. The y position of the airfoil is varied from 1.0D to 1.5D. For the case with y position equal to 1.0D, the jet flow is brushing the airfoil. For the case with y position equal to 1.5D, the interaction is very weak.

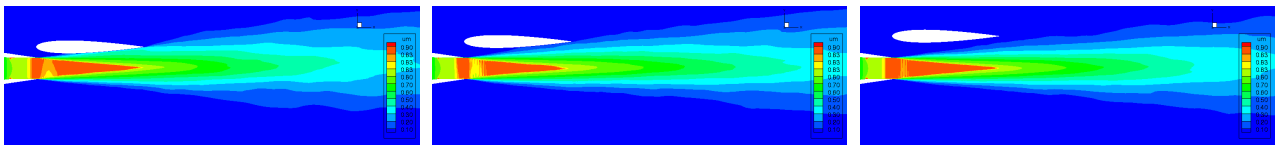

(a) $(0, 1.0D)$ (b) $(0, 1.25D)$ (c) $(0, 1.5D)$

Figure 7: Time averaged mean axial velocity in $x-y$ plane, the airfoil with different radial positions.

The turbulent kinetic energy is computed and plotted. The effect of the airfoil's radial position on the turbulent kinetic energy is shown in Fig. 8. As shown in Fig. 8(a), the turbulent kinetic energy in the shear layer close to the airfoil

DOI: 10.13009/EUCASS2019-1020

is suppressed by the interaction between the jet and the airfoil, but it is amplified in the shear layer of the opposite side. By increasing the gap distance between the airfoil and the jet, the influence of the airfoil on the turbulent kinetic energy is becoming weaker. The distributions of the mean axial velocity along the jet axis are plotted in Fig. 9. In each figure

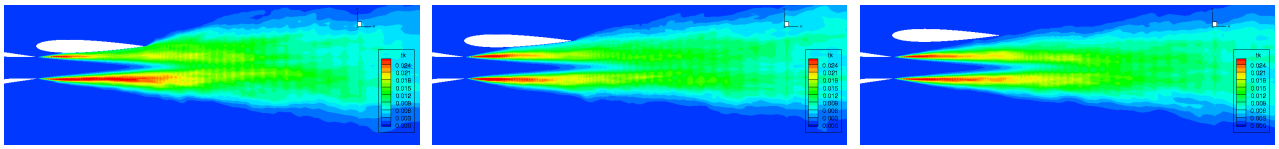

(a) $(0, 1.0D)$ (b) $(0, 1.25D)$ (c) $(0, 1.5D)$

Figure 8: Time averaged turbulent kinetic energy in $x - y$ plane, the airfoil with different radial positions.

the results with different airfoil's radial positions are presented and compared. In Fig. 9(a), it is found that the jet with a larger gap distance has a longer core region for cases of the airfoil's axial position equal to 0. Stronger interaction between the jet and the airfoil enhances the mixing of the shear layer, therefore it shortens the jet core. However, for the cases of the airfoil located 1D downstream, as shown in Fig. 9(b), the jet core length decreases with the increasing of the gap distance. Fixing the radial position of the airfoil to $1.5D$ and varying its axial positions, as shown in Fig. 9(c), the length of the jet core region decreases with the moving downstream of the airfoil because of stronger interaction.

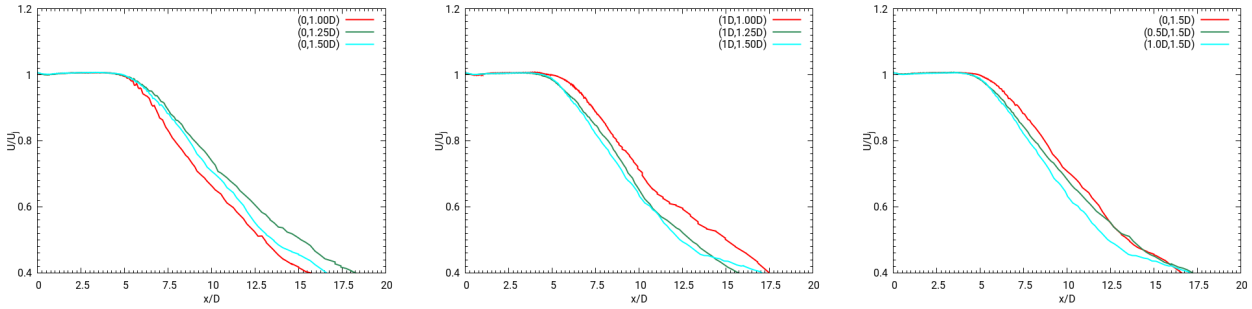

(a) axial position, 0 (b) axial position, $1.0D$ (c) radial position, $1.5D$

Figure 9: Time averaged axial velocity distribution on the jet axis.

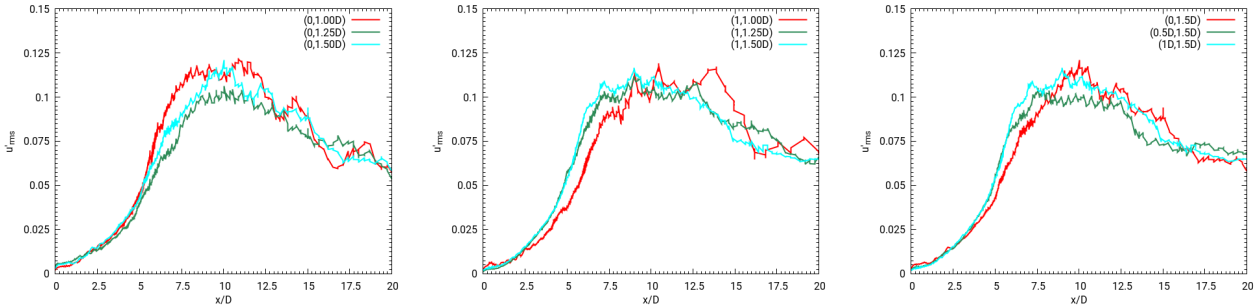

(a) axial position, 0 (b) axial position, $1.0D$ (c) radial position, $1.5D$

Figure 10: The RMS of the velocity perturbations on the jet axis.

The distribution of the RMS of the axial velocity perturbations on the jet axis is plotted in Fig. 10. In Fig. 10(a), it is clear that the distributions of the RMS in the region $[0, 5D]$ have no obvious difference. However, obvious difference can be observed for the results downstream of the airfoil trailing edge. The RMS values of the case with smaller gap distance are much larger because of stronger interaction between the jet and the airfoil, which enhances the jet mixing. However, the conclusion is totally different for the cases of the airfoil located 1D downstream, as shown in Fig. 10(b). The RMS of the velocity perturbations decreases with the increasing of the gap distance. Fixing the radial position of the airfoil to $1.5D$ and varying its axial positions, as shown in Fig. 10(c), it is found that the RMS of the velocity perturbations on the jet axis is larger for case the airfoil with further downstream position.

DOI: 10.13009/EUCASS2019-1020

3.3 Far Field Noise

In this study, the far field noise is obtained with FW-H integration. The position of the integration surface is illustrated in Fig. 11. The surface is extended to about 30D downstream, which is long enough to enclose almost all the noise sources downstream. The end cap of the surface is open in the downstream region to exclude the nonlinear flow field.

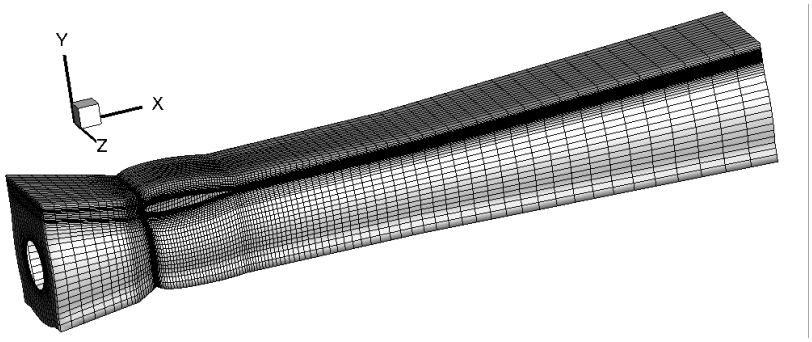

Figure 11: Illustration of the FW-H surface.

The far field noise spectra at $60D$ computed with the FW-H integration method are plotted in Fig. 12 and 13 for the airfoil located at $(0, 1.5D)$ and $(1.0D, 1.0D)$. The numerical results are compared with the experimental data by BUAA.[32] The results at 2 observer angles (0^o from upstream) are presented here, which are 90^o and 150^o respectively. In all these figures, positive observer angle represents the location in the shielded side of the jet, and the negative represents the location in the unshielded side.

The results of the airfoil located at $(0, 1.5D)$ are plotted in Fig. 12. The computed noise spectra agree well with the experimental data with frequency less than 30kHz. The installation effect on the far field noise is predicted correctly both for the shielded and unshielded sides. The noise level in the unshielded side (-90^o and -150^o) is much larger than that on the shielded side (90^o and 150^o), especially at the observer angle 90^o. This means the installed NACA0012 airfoil has larger effect on the side-line noise than the downstream.

The results of the airfoil located at $(1.0D, 1.0D)$ are plotted in Fig. 13. The predicted results are compared with the experimental data, and the conclusion is similar with the case shown in Fig. 12. It can also be found that for this case the difference between the downstream noise spectra (150^o) on the shielded and unshielded sides is much clearer than the case with larger gap distance, for instance, the spectra shown in Fig. 12(b). This means the installation effect on the downstream noise spectra is larger with the decreasing of gap distance.

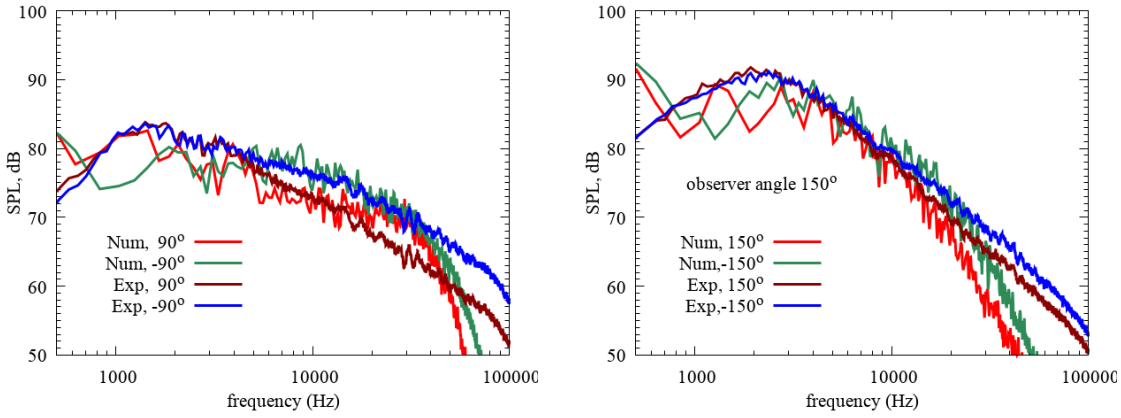

(a) 90^o (b) 150^o

Figure 12: Far field noise spectra of the jet/airfoil interaction($r/D = 60$), airfoil position $(0, 1.5D)$.

The effect of the airfoil's radial position on the far field noise spectra is shown in Fig. 14. The noise level decreases with the gap distance between the jet and the airfoil. It is true both for the 90^o and 150^o observer angles on the shielded and unshielded sides. The effect of the radial position on the noise spectra is larger for the observer point on the shielded side than that on the unshielded side, which are shown clearly in Fig. 14(a) and 14(c).

DOI: 10.13009/EUCASS2019-1020

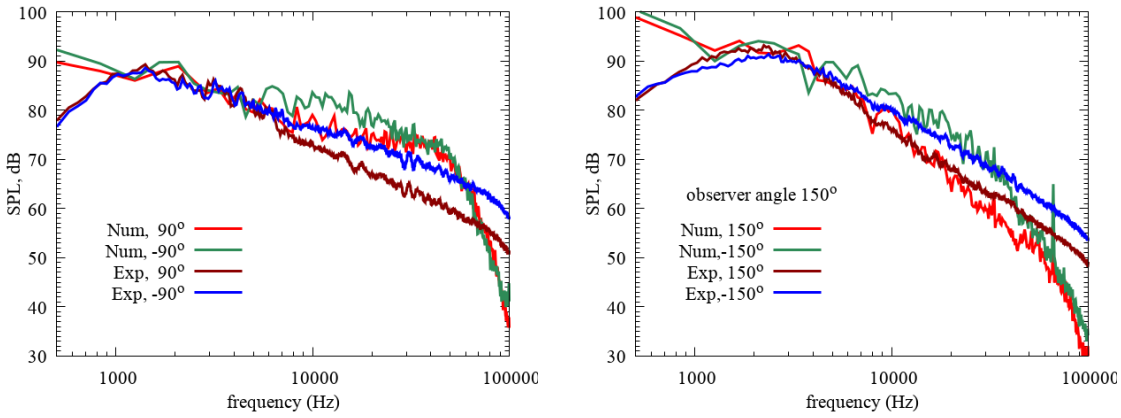

(a) 90^o (b) 150^o

Figure 13: Far field noise spectra of the jet/airfoil interaction($r/D = 60$), airfoil position $(1.0D, 1.0D)$.

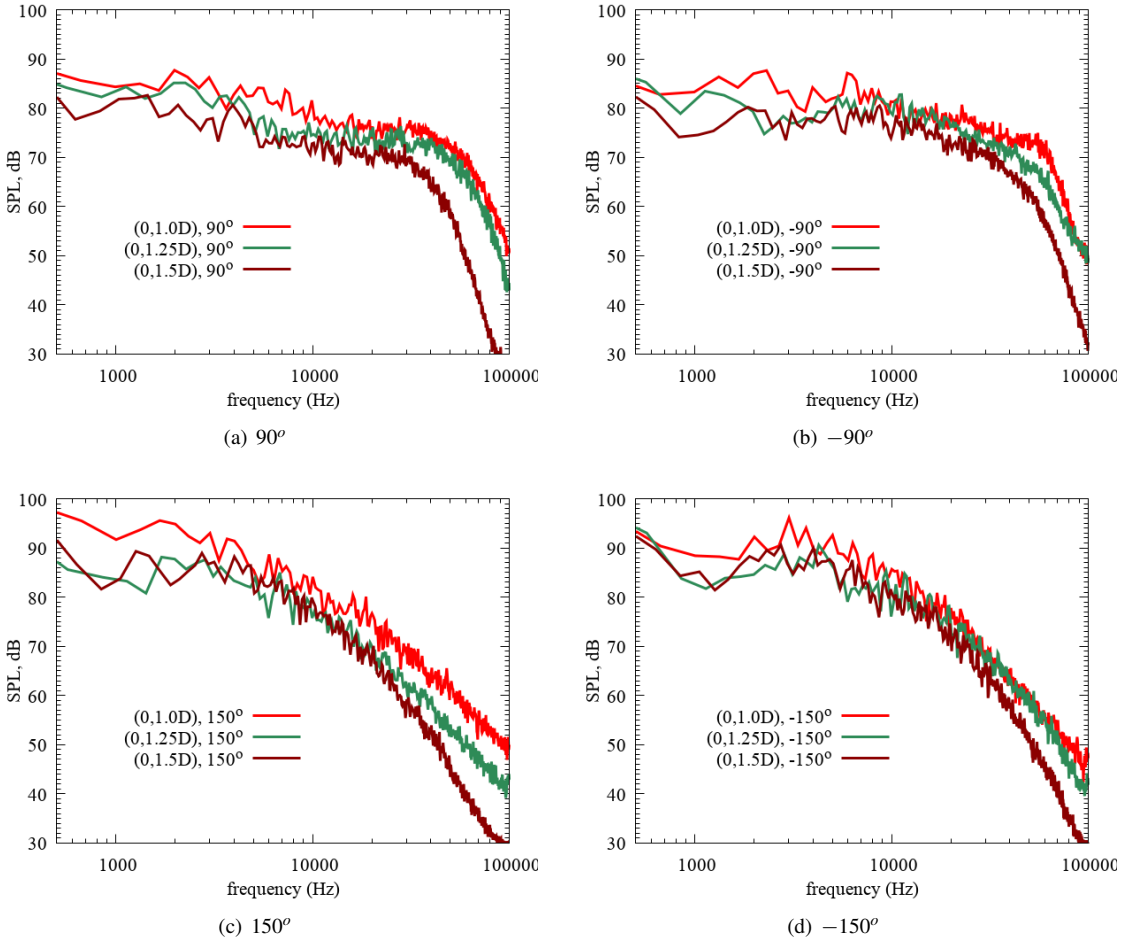

(a) 90^o (b) -90^o

(c) 150^o (d) -150^o

Figure 14: The effect of the airfoil's radial positions on the far field noise spectra.

DOI: 10.13009/EUCASS2019-1020

The OASPL at $r = 60D$ is computed and presented in Fig. 15. The directivity of the far field noise ($r = 60D$) is plotted in Fig. 15. The OASPL at all observer angles decreases with the gap distance inversely, as shown in Fig. 15(a). The OASPL at all observer angles increases with the downstream distance of the airfoil, as shown in Fig. 15(b).

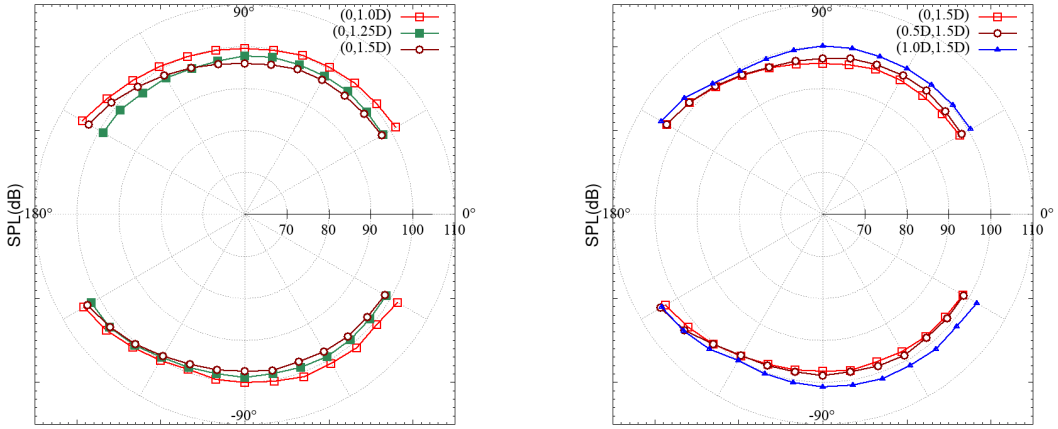

(a) airfoil position, $x = 0$

(b) airfoil position, $y = 1.5D$

Figure 15: OASPL at $60D$

4. Conclusions

In this study, the jet noise with installation effect is simulated with a high order computational aeroacoustics solver. A convergent nozzle with exit diameter equal to $2.54cm$ is placed under a NACA0012 airfoil. The influence of their relative positions is studied by changing the location of the airfoil both in the x and radial directions. The flow fields, including the mean axial velocity, turbulent kinetic energy, and the RMS of the velocity perturbations are analyzed to show the installation effect. It is found that smaller gap distance between the jet and the airfoil leads to stronger interaction, and this results in shorter jet core region and larger turbulent kinetic energy downstream of the airfoil trailing edge. The far field noise spectra at different observer angles are computed and compared with the experimental data. Good agreements with the frequency less than 30kHz are obtained for observer points on the shielded and unshielded sides of the jet. The effect of the axial and radial positions of the airfoil on the far field noise are presented and analyzed. It is found that the OASPL at all observer angles decreases with the radial gap distance inversely, but increases with the axial distance of the airfoil.

5. Acknowledgments

This work is supported by grants from NSFC-51876003, 91752204, Key Laboratory of Aerodynamic Noise Control (ANCL20170301), the Europe and China collaboration project “Innovative Methodologies and Technologies for Reducing Aircraft Noise Generation and Emission (IMAGE)”, and the 111 project of Beihang University (B07009).

References

[1] K. V. Abeele, T. Broeckhoven, and C. Lacor. Dispersion and dissipation properties of the 1D spectral volume method and application to p-multigrid algorithm. *Journal of Computational Physics*, 224:616–636, 2007.

[2] C. Bogey and C. Bailly. Three-dimensional non-reflective boundary conditions for acoustic simulations: Far field formulation and validation test cases. *ACTA Acustica United With Acustica*, 88:463–471, 2002.

[3] K.S. Brentner and F. Farassat. Analytical comparison of the acoustic analogy and Kirchhoff formulation for moving surfaces. *AIAA Journal*, 36(8):1379–1386, 1998.

[4] W. H. Brown and K. K. Ahuja. Jet and wing/flap interaction noise. 9th AIAA Aeroacoustics Conference, AIAA Paper 1984–2362, 1984.

DOI: 10.13009/EUCASS2019-1020

[5] M. J. Fisher, M. Harper-Bourne, and S. A. L. Glegg. Jet engine noise source location: the polar correlation technique. *Journal of Sound and Vibration*, 51:23–54, 1977.

[6] J. H. Gao and X. D. Li. Detached eddy simulation of flow over naca0012 airfoil at high angle of attack with spectral difference method. In *52nd AIAA Aerospace Sciences Meeting*, AIAA Paper 2014–0425, 2014.

[7] J. H. Gao and X. D. Li. A multi-time-step spectral difference solver for multiple-scales aeroacoustics problems. In *the 21st International Congress on Sound and Vibration, July 13-17, 2014, Beijing, China.*, 2014.

[8] J. H. Gao, X. D. Li, and D.K. Lin. Numerical simulation of the noise from the 30P30N highlift airfoil with spectral difference method. In *23rd AIAA/CEAS Aeroacoustics Conference*, AIAA Paper 2017–3363, 2017.

[9] J. H. Gao and X.D. Li. Numerical simulation of the noise from a subsonic jet in static and flight conditions. 25th AIAA/CEAS Aeroacoustics Conference, AIAA Paper 2019–2666, 2019.

[10] J.H. Gao and X.D. Li. Implementation of delayed detached eddy simulation method to a high order spectral difference solver. *Computers and Fluids*, 154:90–101, 2017.

[11] R. Head and M. Fisher. Jet surface interaction noise - analysis of far-field low frequency augmentations of jet noise due to the presence of a solid shield. AIAA Paper 1976–502, 1976.

[12] F. Q. Hu. On the construction of pml absorbing boundary condition for the non-linear Euler equations. AIAA Paper 2006–798, 2006.

[13] F. Q. Hu, M. Y. Hussaini, and J. L. Manthey. Low-dissipation and low-dispersion Runge-Kutta schemes for computational acoustics. *Journal of Computational Physics*, 124(1):177–191, 1996.

[14] H. T. Huynh. A flux reconstruction approach to high-order schemes including discontinuous galerkin methods. AIAA Paper 2007–4079, 2007.

[15] X. D. Li and J. H. Gao. Numerical simulation of the three dimensional screech phenomenon from a circular jet. *Physics of Fluids*, 20:035101, 2008.

[16] C. L. Liang, S. Premasuthan, A. Jameson, and Z. J. Wang. Large eddy simulation of compressible turbulent channel flow with spectral difference method. AIAA Paper 2009–402, 2009.

[17] D.K. Lin, M. Jiang, and X.D. Li. A multi-time-step strategy based on an optimized time interpolation scheme for overset grids. *Journal of Computational Acoustics*, 18:131–148, 2010.

[18] C. J. Mead and P. J. R. Strange. Under-wing installation effects on jet noise at sideline. AIAA Paper 1998–2208, 1998.

[19] F. Nicoud and F. Ducros. Subgrid-scale stress modeling based on the square of the velocity gradient tensor. *Flow, Turbulence and Combustion*, 62:183–200, 1999.

[20] D. Papamoschou and S. Mayoral. Experiments on shielding of jet noise by airframe surfaces. AIAA Paper 2009–3326, 2009.

[21] N.N Pastouchenko and C.K.W. Tam. Installation effects on the flow and noise of wing mounted jets. *AIAA Journal*, 45(12):2851–2860, 2007.

[22] L. Rego, F. Avallone, D. Ragni, and D. Casalino. Free-stream effects on jet-installation noise of a dual-stream engine. 25th AIAA/CEAS Aeroacoustics Conference, AIAA Paper 2019–2491, 2019.

[23] M. Reshotko, J.H. Goodykoontz, and R.G. Dorsch. Engine-over-the-wing noise research. NASA TM–X–68246, 1973.

[24] V.V. Rusanov. Calculation of interaction of non-steady shock waves with obstacles. *Journal of Computational Math Physics*, USSR 1:261–279, 1961.

[25] Y. Sun, Z. J. Wang, and Y. Liu. High-order multidomain spectral difference method for the navier-stokes equations on unstructured hexahedral grids. *Communications in Computational Physics*, 5:760–778, 2009.

[26] C. K. W. Tam and Z. Dong. Radiation and outflow boundary conditions for direct computation of acoustic and flow disturbances in a nonuniform mean flow. *Journal of Computational Acoustics*, 4:175–201, 1996.

DOI: 10.13009/EUCASS2019-1020

[27] C. K. W. Tam and J. C. Webb. Dispersion-relation-preserving finite difference schemes for computational acoustics. *Journal of Computational Physics*, 107:262–281, 1993.

[28] U. Von Glahn, J. Goodykoontz, and J. Wagner. Nozzle geometry and forward velocity effects on noise for CTOL engine-over-the-wing concept. NASA TM–X–71453, 1973.

[29] U. Von Glahn, D. Groesbeck, and M. Reshotko. Geometry considerations for jet noise shielding with CTOL engine-over-the-wing concept. AIAA Paper 1974–568, 1974.

[30] U. Von Glahn, D. Groesbeck, and J. Wagner. Wing shielding of high-velocity jet and shock-associated noise with cold and hot flow jets. AIAA Paper 1976–547, 1976.

[31] M. E. Wang. Wing effect on jet noise propagation. AIAA Paper 1980–1047, 1980.

[32] X. H. Xu and X.D. Li. Experimental research of installed jet noise. 25th AIAA/CEAS Aeroacoustics Conference, AIAA Paper 2019–2634, 2019.